

Operando HERFD-XAS of Bimetallic Perovskite Thin Film Interfaces

Qijun Che,* Iris C. G. van den Bosch, Jelle R. H. Ruiters, Yuang Piao, Christoph Baeumer,*
Pieter Glatzel, Danilo Kühn, and Frank M. F. de Groot*



Cite This: *J. Am. Chem. Soc.* 2026, 148, 414–424



Read Online

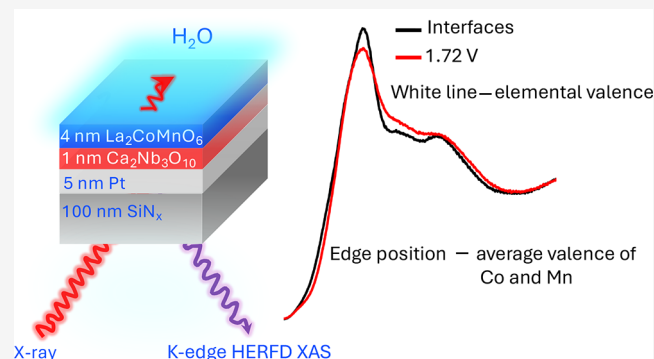
ACCESS |

Metrics & More

Article Recommendations

Supporting Information

ABSTRACT: We investigated the valence dynamics of thin films during the electrocatalytic oxygen evolution reaction using operando high-energy-resolution fluorescence-detected (HERFD) X-ray absorption spectroscopy (XAS) in a 0.1 M KOH solution under an applied potential. We show that it is possible to measure the 10 unit cell (~4 nm) bimetallic perovskite oxide $\text{La}_2\text{CoMnO}_6$ thin film grown on Pt-covered SiN_x membranes. Operando Co and Mn K-edge HERFD XAS spectra on the active surface species were recorded from the backside of the SiN_x membrane. The HERFD XAS Co K-edge spectra reveal a (partial) increase in the oxidation state from Co^{2+} in ex situ conditions to mainly Co^{3+} in the solid–liquid open-circuit voltage (OCV). Voltage-dependent Co K-edge HERFD XAS white line intensities show that Co is oxidized toward the higher oxidation state, while Mn remains Mn^{4+} . Interestingly, the Co and Mn main edge shifts with the average valence change of 0.20; the valence of Mn is constant, implying that the valence of Co increases by 0.40. The OCV spectra were reversible when switching off the potentials. These observations clearly identify element-specific valence dynamics in the intrinsic oxygen evolution reaction.



INTRODUCTION

The development of sustainable energy is essential to reduce reliance on nonrenewable natural resources and prevent environmental pollution.¹ The (photo)electrochemical technology for producing hydrogen (or chemical fuels) and oxygen presents an ideal pathway for the storage and conversion of renewable energy. A critical step in this process is the electrocatalytic oxygen evolution reaction (OER; $4\text{OH}^- \rightarrow \text{O}_2 + 2\text{H}_2\text{O} + 4\text{e}^-$ in alkaline media).^{2,3} The OER involves a complex 4-electron transfer process, leading to significant kinetic bottlenecks,⁴ since it requires large applied overpotential ($\eta_{\text{OER}} > 0.3$ V), which hampers efficiency.⁵ To address these challenges, electrocatalysts with high activity, long-term durability, and low cost have been developed, including transition metal oxides.^{6–8}

Despite the promise of various electrocatalysts, the mechanism of the OER remains unclear. The conventional mechanism, known as the adsorbate evolution mechanism, involves four concerted proton–electron transfer steps at surface metal-ion centers.^{9–11} This mechanism is characterized by moderate binding strength of intermediates on the metal surface and exhibits pH-independent activity, supported by experiments that estimate electronic structure parameters such as e_g occupations.⁶ Recently, the lattice oxygen-mediated mechanism has been proposed as an alternative, supported by several observations: (1) some active metal oxides demonstrate pH-dependent OER activity,^{12–14} (2) bulk electronic structure modifications in

perovskites, such as metal–oxygen hybridizations, enhance OER activities and kinetics,^{15–18} and (3) electrochemical mass spectrometry studies of bulk oxides including NiCo_2O_4 ¹⁹ and ¹⁸O-labeled perovskites like $\text{La}_{0.5}\text{Sr}_{0.5}\text{CoO}_{3-\delta}$ and $\text{SrCoO}_{3-\delta}$ have revealed that oxygen molecules can originate not only from water but also from the lattice oxygen of the transition metal oxides.^{3,20–22}

Understanding the electronic structures—such as spin, oxidation state, covalence, and charge-transfer energy parameters of electrocatalysts—is crucial, especially under *in situ* and *operando* conditions.^{23,24} Reported *operando* studies often involve nanoparticles (or thin films) that can undergo structure-phase transformations or reconstructions, forming metal-(oxy)hydroxides.^{25–31} These investigations contain controversies regarding the +4 valence state that is potentially formed during electrocatalysis. Compounds like LaNiO_3 ³² and SrCoO_3 ^{33,34} are known as negative charge-transfer systems. In the case of Co^{4+} , the ground state is mainly characterized by the $3d^6L$ configuration, where L indicates a ligand (oxygen) hole in

Received: August 13, 2025

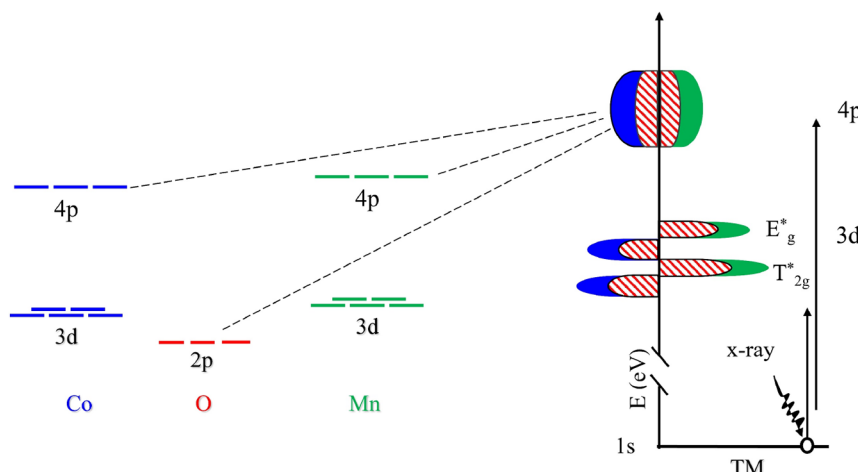
Revised: December 11, 2025

Accepted: December 15, 2025

Published: January 2, 2026



Scheme 1. Diagram Illustrates TM 1s (K-Edge) XAS to the Empty 3d + 4p Band, with Blue Indicating Co, Green Indicating Mn, and Red Indicating Oxygen Contributions



^a $E_g^* - T_{2g}^*$ indicates the crystal field splitting (10 Dq). The 4p band forms as a mixture of the Co and Mn 4p states that are coupled with the oxygen 2p states.

the ligand valence band, with the charge-transfer energy (Δ_{ct}) defined as the energy difference between the $3^{N+1}L$ and $3d^N$ configurations.³⁵ The presence of a ligand hole reflects strong metal–ligand covalency and a reduction of the formal electron deficiency in the transition metal 3d states.

Lanthanide-based perovskites are ideal for studying electrocatalysis due to their well-defined crystal structure and stability of the bulk crystalline phase under reaction conditions.³⁶ Such stability makes them suitable models for probing the effects of near-surface transformations. Epitaxially grown, smooth perovskite thin films on single-crystal substrates that expose a single crystallographic facet to the electrolyte have been extensively investigated for OER studies.^{37–40} Recently, we demonstrated that combining pulsed laser deposition (PLD) of perovskite thin films onto a monolayer $\text{Ca}_2\text{Nb}_3\text{O}_{10}$ nanosheet-buffered SiN_x membrane with conductive layers enables successful operando XAS measurements from the membrane's backside.⁴¹ To investigate the valence state and covalence dynamics of transition metal ions with both low and high oxidation states, we study double perovskite oxides that simultaneously contain these oxidation states. Specifically, we focus on the $\text{La}_2\text{CoMnO}_6$ perovskite oxide. $\text{La}_2\text{CoMnO}_6$ contains a mixture of octahedral (O_h) high-spin Co^{2+} ($3d^7, t_{2g}^5 e_g^2, S = 3/2$) combined with a Mn^{4+} ($3d^3, t_{2g}^3 e_g^0, S = 3/2$) state, with a Curie temperature (T_C) between 240 and 322 K.^{42–44} Using PLD, we grow 10 unit cells (u.c.) $\text{La}_2\text{CoMnO}_6$ thin films on monolayer $\text{Ca}_2\text{Nb}_3\text{O}_{10}$ (CNO) nanosheets-buffered 5 nm Pt-covered SiN_x membranes for operando studies.

Operando high-energy-resolution fluorescence detection (HERFD) XAS is highly effective for probing the electronic structure, surpassing traditional XAS techniques. HERFD XAS minimizes spectral broadening caused by effectively removing the short lifetime of the 1s core state, allowing for improved effective resolution.^{45,46} Typically, K_α (1s2p) or K_β (1s3p) X-ray emission lines are used, with the K_α channel being preferred for thin film measurements due to its higher intensity. HERFD XAS at the transition metal (TM) K-edge provides detailed information about the electronic structure and the geometry. This includes insights into oxidation states, local symmetry, spin states, and crystal-field splitting.

We will define the bonding of the metal 3d and 4p bands in order to explain the operando HERFD XAS changes observed in the $\text{La}_2\text{CoMnO}_6$ thin film oxides. As illustrated in Scheme 1, 1s XAS probes the unoccupied 3d and 4p band. The 3d band, which consists of TM 3d ($e_g + t_{2g}$) orbitals hybridized with O 2p, and the 4p band, which involves TM 4p hybridized with O 2p, reflect the covalence or TM–O bonding. For simplicity, we ignore the 4s orbitals. Ionic Co (blue lines) and Mn (green lines) interact with oxygen (red lines) resulting in the following aspects of the electronic structure: the TM ground state has the main bonding between oxygen 2p and metal 4p orbitals creating the bonding oxygen 2p valence band and the antibonding metal 4p band (t_{1u}). In addition, there is the bonding between oxygen 2p and metal 3d orbitals contributing to the bonding oxygen 2p band and creating the antibonding metal 3d band, which is split into the sharp t_{2g} -band (π antibonding) and the broader e_g -band (σ antibonding), split by a crystal field. We will argue in the 8 points below that the pre-edge follows the elemental oxidation state but that the edge can follow the average oxidation state of the two metals.

- (1) Experimental evidence shows that for octahedral binary oxides, the pre-edge position shifts linearly by ~1.3 eV/valence and the edge position by 2.5 to 3.5 eV/valence, as clearly indicated, for example, by Wong et al.⁴⁷
- (2) The reason for this constant shift can be related to the chemical bonding; the pre-edge position is determined by the energy position of the antibonding combination of the oxygen 2p and metal 3d orbitals, while the edge position can (in first approximation) be assigned to the energy position of the antibonding combination of the oxygen 2p and metal 4p orbitals. An increase in valence implies a decrease of the metal–oxygen bond distance and an increase of the chemical bonding. A wide range of experiments have shown that the energy positions of antibonding state scale linearly with the formal valence.
- (3) In case of oxides that contain more elements, there are variations for the same formal valence. A clear example is the shifts of the L_3 maximum for Cu^{2+} oxides that vary by 1 eV, where the lowest peak position relates to systems with the longest Cu–O bond distance.⁴⁸ In case of different

- ligands than oxygen, different metal spin-states, or different metal coordination, there are variations in the (pre)-edge position for the same valence.
- (4) Consider the density of states of an oxide with two transition metal ions. The energy positions of the 3d states of both ions are given by the antibonding combination of the oxygen 2p and metal 3d orbitals of each metal separately. However, the 4p bands of such systems have bands that are delocalized and its energy position is given by the antibonding combination of the oxygen 2p and metal 4p orbitals of both metals (**Scheme 1**).
 - (5) In case of K-edges, there is a core hole effect that will create element-specific (excitonic) states for the 3d states, but for the joined 4p states, it will pull states of the excited element to the bottom of the band. Assuming that the core hole effect of both elements is equivalent, one can assume that the first K-edge peak reaches the same states for both elements.
 - (6) The energy position of the 3d band is element-specific, but the energy position of the joined metal 4p band is defined by both metals, and if one of the two metals changes its valence, the K-edge of both metals shifts similarly. In case of Co and Mn, we thus expect that if the Co valence increases, the joined 4p band shifts up and the edge position of both Co and Mn will shift up.
 - (7) Because this effect depends on the antibonding mixed-metal 4p band, it will depend on the crystal symmetry to determine how well the states are mixed and if this argument will hold. We expect that there are two extreme cases: (a) the edge follows the elemental valence and (b) the edge follows the joined valence. In the present case of perovskite systems, the experimental data suggests that the situation is close to the limit where the edge follows the joined valence. In case that one combines more different types of metals, for example, a 3d element with a 5d element, the mixing of the band structure can be expected to be more complex, and the edge might follow more closely the position of the individual ions.
 - (8) Systematic experimental data and DFT calculations could distinguish both cases for a range of systems.

■ EXPERIMENTAL SECTION

Perovskite $\text{La}_2\text{CoMnO}_6$ Thin Film Fabrications

10 u.c. (i.e., ~4 nm) perovskite $\text{La}_2\text{CoMnO}_6$ thin films were fabricated using pulsed laser deposition (PLD), following a method like our previous report.⁴¹ Two-dimensional monolayer CNO nanosheets, with a thickness of 1–2 nm, were deposited on Pt/SiN_x membranes using the Langmuir–Blodgett method, as described in ref 49. The SiN_x membranes were purchased from Silson Ltd. (Southam, UK) with a frame size of 10 mm × 10 mm × 525 μm and a center membrane size of 2.5 mm × 2.5 mm × 100 nm. 5 nm Pt was sputter-deposited on the SiN_x membrane before CNO deposition. The thickness was chosen as a compromise to allow for sufficient conductivity, stability during the PLD process, and maximum X-ray transparency. $\text{La}_2\text{CoMnO}_6$ thin films were grown on the CNO-buffered Pt/SiN_x membranes using PLD with a KrF excimer laser source at 248 nm, yielding locally epitaxial growth on each individual nanosheet and an overall film with single out-of-plane (001) orientation in pseudocubic notation of the $\text{La}_2\text{CoMnO}_6$ unit cell. The growth conditions were as follows: laser fluence of 1.8 J/cm², frequency of 2 Hz, spot size of 1.76 mm², deposition temperature of 650 °C, oxygen partial pressure (p_{O_2}) of 0.04 mbar, and target-to-substrate distance of 5 cm. The process included heating at 8 °C per minute in 0.04 mbar O₂, annealing for 1 h in 0.04 mbar O₂ to stabilize the membrane, and cooling down at 8 °C per minute.

Physical Characterization

Atomic force microscopy (AFM) on a Bruker Dimension Icon with a TESPA-V2 probe in tapping mode was employed to monitor the surface morphology, with data analysis conducted using the Gwyddion software package.⁵⁰ X-ray diffraction (XRD) on a Bruker D8 Discover X-ray diffractometer was used to characterize the crystal structure of the $\text{La}_2\text{CoMnO}_6$ thin films grown on CNO-buffered Pt/Si. Symmetrical scans were recorded using the large area detector in 1D mode to capture the in-plane random oriented crystals on the nanosheets.

Ex Situ Soft X-ray XAS Measurements

Ex situ soft X-ray XAS measurements of $\text{La}_2\text{CoMnO}_6$ thin films for Co 2p XAS and Mn 2p XAS are conducted at the COESCA station at the UE52-PGM undulator beamline of the BESSY II synchrotron at room temperature (25 °C). The signals were recorded by total electron yields.

Operando HERFD XAS Measurements

We conducted operando HERFD XAS experiments using a custom-built operando reactor. The reactor is equipped with three electrodes: a working electrode (the membrane samples), a reference electrode (Leakless Miniature Ag/AgCl Reference Electrode, eDAQ, Australia), and a counter electrode (Pt). The operando electrocatalysis was performed using a BioLogic SP-200 potentiostat (BioLogic Science Instruments, France). To minimize the impact of oxygen bubbles, a continuous flow of a 0.1 M KOH solution was used. The alkaline solution was prepared by dissolving KOH pellets (Sigma-Aldrich, 99.99%) in Milli-Q water. All electrochemical potentials are measured relative to the Ag/AgCl reference electrode at a room temperature of 25 °C (see below),⁵¹ which are further converted to the reversible hydrogen electrode (RHE) and corrected for the uncompensated resistance drop via $V_{\text{vs RHE}}(V) = V_{\text{Ag/AgCl}} + 0.197 + 0.0592 \text{ pH} - iR_s$, where the i is the current and R_s is the solution ohmic resistances obtained from electrochemical impedance spectroscopy (Figure S1), assuming that the pH is 13.

The operando HERFD XAS measurements are performed at beamline ID26 of the European Synchrotron Radiation Facility (ESRF).^{52,53} For the experiments, five analyzers were employed: three Si 531 analyzers for Co and two Ge 333 analyzers for Mn. The Co K α (1s2p) and Mn K α (1s2p) X-ray emission channels were used for detection. The combined (incoming and outgoing) X-ray energy resolution was about 0.7 eV for Mn and Co.⁵³ The photon energy step was set to 0.1 eV, and a quick scan time of 60 s was used for both Co and Mn K-edge HERFD XAS measurements. Standard reference samples of MnO, Mn₂O₃, CoO, and Co₃O₄ (99.99% purity) purchased from Sigma-Aldrich and made into pellets were also measured. MnO pellets were tracked for their HERFD XAS before operando and after operando experiments. No energy shifts were detected (Figure S2). The operando measurement procedures are as follows:

- (i) Ex situ 1. (a) Homogeneity studies: 24 spots across of the $\text{La}_2\text{CoMnO}_6$ thin films membrane are selected with each spot shifted over the x - or y -axes by 100 μm. For each spot, 5 cycle scans were performed for Co and Mn K-edge XAS. No inhomogeneity was detected in thin films based on the XAS spectra (Figure S3). (b) Beam damage study: A single spot on the sample was subjected to 50 cycle scans for both Mn and Co K-edges to assess potential damage with each scan taking 60 s. No visible X-ray damage was observed on the films or in the spectra (Figure S4), indicating the robustness of the sample under prolonged XAS measurements.

The next protocol for both the Co and Mn K-edge HERFD XAS was to select 5 spots on the sample and perform 22 cycle scans per spot, each scan taking 40 s to avoid beam damage and to obtain optimal signal/background data. Each spectrum of Co/Mn takes approximately 1 h and 40 min.

- (ii) OCV1 XAS. The sample is stabilized at open-circuit voltage (OCV) for 15 min, after which potentiodynamic impedance spectroscopy (PEIS) is carried out to check the electrical connections to the cell and to determine the uncompensated resistance. Then the protocol for collecting

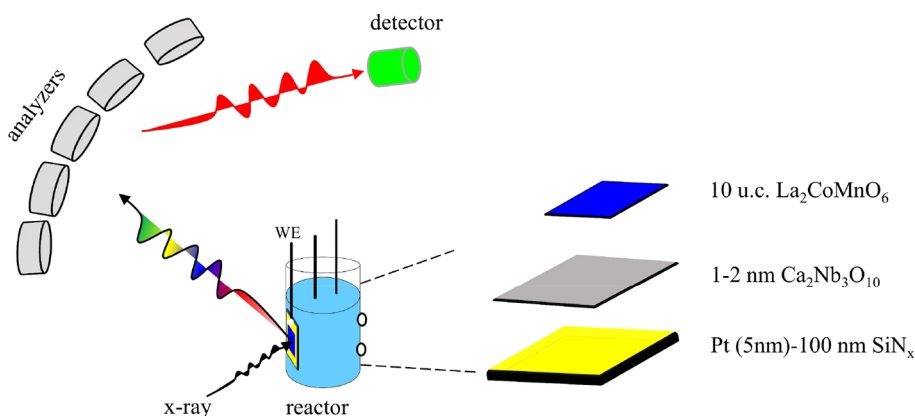


Figure 1. A scheme of the operando HERFD XAS experimental setup with 10 u.c. $\text{La}_2\text{CoMnO}_6$ thin films; CNO indicates a monolayer of $\text{Ca}_2\text{Nb}_3\text{O}_{10}$ nanosheets with 1–2 nm thickness.

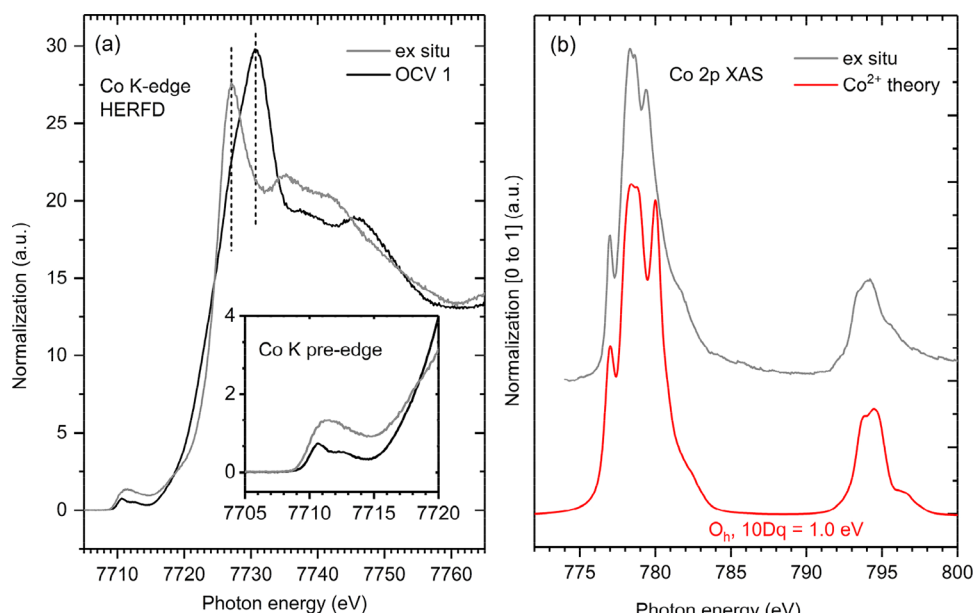


Figure 2. (a) Environment-dependent Co K-edge HERFD XAS spectra of $\text{La}_2\text{CoMnO}_6$ under different conditions: ex situ and in alkaline liquid (OCV1); inset: enlarged view of Co K pre-edge spectra. (b) Ex situ Co 2p XAS of 10 u.c. $\text{La}_2\text{CoMnO}_6$ and theoretical Co^{2+} 2p XAS by charge-transfer multiplet simulations.

Co and Mn K-edge HERFD XAS was started, while keeping the cell at OCV (no applied potential).

- (iii) Electrochemical characterization. After collecting the XAS spectra, a sequence of subsequent electrochemical characterization is conducted through recording of PEIS at OCV, CV (0.1 to 0.3 V vs $V_{\text{Ag}/\text{AgCl}}$), and CV (0.3 to 0.6 V vs $V_{\text{Ag}/\text{AgCl}}$) and PEIS at OCV. The CV cycles are recorded with a scan rate of 10 mV/s, 30 mV/s, 50 mV/s, 70 mV/s, 100 mV/s, 150 mV/s, 200 mV/s, 250 mV/s, 300 mV/s, 350 mV/s, 400 mV/s, 450 mV/s, and 500 mV/s, with two sweeps per scan rate.
- (iv) Modular potentiostatic (MP) technique. After step (iii), MP is conducted. In the MP setup, 5 sweeps to a maximum current density of 1 mA/cm² and back to OCV are conducted with 10 mV/s to assess electrocatalytic OER performance. With the MP technique, voltage-dependent steps are chosen to conduct the voltage-dependent HERFD XAS.
- (v) Voltage-dependent HERFD XAS. Linear Sweep Voltammetry (LSV) is used from OCV to 0.55 V (vs $V_{\text{Ag}/\text{AgCl}}$), to 0.7 V, and to 0.78 V, with a scan rate of 10 mV/s. The separate LSV measurements are followed by chronoamperometry (CA) measurements, with a 15 min stabilization time and followed by a PEIS measurement, after which the protocol for collecting

Co and Mn K-edge HERFD XAS was started (while holding at the chosen potentials). In addition, frequent PEIS measurements were conducted during potential holds.

- (vi) OCV2 XAS. LSV is used from 0.78 V (vs $V_{\text{Ag}/\text{AgCl}}$) to OCV, followed by 15 min stabilization and PEIS, then the protocol for collecting Co and Mn K-edge HERFD XAS was started. This data point will be used to check reversibility of the sample after being at OER conditions.
- (vii) Higher voltage-dependent HERFD XAS and OCV3 XAS. The same procedure as mentioned in (ii–vi) is used to conduct XAS measurements at higher potentials. Here, the Co and Mn K-edge HERFD XAS is collected at 0.855 V vs $V_{\text{Ag}/\text{AgCl}}$ and 0.93 V vs $V_{\text{Ag}/\text{AgCl}}$.
- (viii) Ex situ 2. When the liquid is removed, ex situ HERFD XAS is measured again to compare with ex situ 1.
- (ix) Data analysis. Each spectrum is processed by subtracting the baseline offset and normalizing it to the integrated area, with a Python function of $(y - \min(y)) / \text{trapezoid}(\max(y) - \min(y), x)$. Due to the dilute nature of the sample, consisting of only 10 unit cells (u.c.), self-absorption and saturation effects are negligible when using the 1s2p X-ray emission channel.^{54,55}

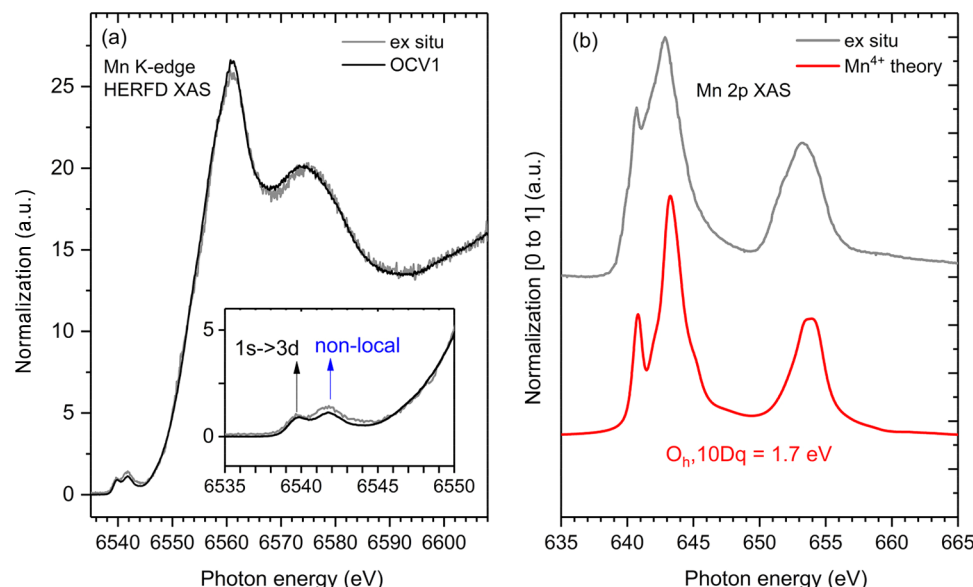


Figure 3. (a) Environment-dependent Mn K-edge HERFD XAS spectra of $\text{La}_2\text{CoMnO}_6$ ex situ (in air) and OCV1 (in alkaline liquid); inset: enlarged Mn K pre-edge. (b) Ex situ Mn 2p XAS of 10 u.c. $\text{La}_2\text{CoMnO}_6$ and theoretical Mn^{4+} 2p XAS by charge-transfer multiplet simulations.

RESULTS

Figure 1 presents the operando HERFD XAS experimental setup associated with 10 u.c. $\text{La}_2\text{CoMnO}_6$ thin films as well as the X-ray signal detected from the backside of the SiN_x membrane (see the Experimental Section for details).

ENVIRONMENT-DEPENDENT XAS SPECTRA

We first address the prestudy concerning the homogeneity and potential X-ray damage to the thin films. Our observations confirm that there are no inhomogeneities or beam damage that affects the samples.

Figure 2a displays the environment-dependent Co K-edge HERFD XAS spectra of the $\text{La}_2\text{CoMnO}_6$ thin films. The ex situ condition refers to measurements taken in air (without an alkaline liquid), while the OCV condition corresponds to the sample being exposed to the liquid electrolyte without an applied potential. The ex situ Co K-edge XAS of 10 u.c. $\text{La}_2\text{CoMnO}_6$ thin films is expected to contain Co^{2+} .^{42–44} Figure 2b displays the Co 2p XAS of 10 u.c. $\text{La}_2\text{CoMnO}_6$ and Co^{2+} 2p XAS charge-transfer multiplet simulations. The theoretical Co^{2+} XAS spectra in octahedral coordination have been investigated using a Quanty script with the parameters from ref 56. The theoretical Co^{2+} 2p XAS spectra match well with experimental observation, confirming a Co^{2+} valence state in the 10 u.c. $\text{La}_2\text{CoMnO}_6$ thin films. The OCV1 Co K-edge HERFD XAS spectrum shows a white line positive shift of ~ 3.63 eV relative to the ex situ conditions. This white line position and shape is similar to Co^{3+} in cobalt oxyhydroxide.²⁶ In addition, the first derivative maximum peak shifts ~ 0.9 eV compared to the ex situ condition (Figure S5), which suggests a (partial) Co-oxidation from Co^{2+} to Co^{3+} .^{28,57} Identifying the Co pre-edge fine structures is complex due to the overlapping effects of the 1s to 3d quadrupole transition, the local 3d/4p state mixture, and nonlocal Co 4p–(O 2p–Mn/Co 3d) states. The octahedral (O_h) high-spin (HS) Co^{2+} of CoO only shows 1s to 3d quadrupole transition without showing a local 3d/4p mixture (due to O_h symmetry) and without visible nonlocal peaks (due to relatively long Co–O bonds⁵⁸). Co^{2+} in the perovskite $\text{La}_2\text{CoMnO}_6$ oxides also has O_h symmetry (Figure 2b).^{42–44} But

in comparison with CoO , the Co pre-edge of $\text{La}_2\text{CoMnO}_6$ shows a broader peak (full width 6.2 eV vs 4.7 eV in CoO).⁵⁸ This broadening is attributed to nonlocal peaks due to Co 4p–(O 2p–Mn 3d) overlap, visible due to the short Mn–O bonds of the Mn^{4+} ions (see below).^{59–61} Additionally, the energy resolution of ~ 0.7 eV full width at half-maximum (fwhm) in $\text{La}_2\text{CoMnO}_6$ thin films is lower (by 0.4 eV) than ref 58, implying that the crystal field multiplet fine structure at the Co pre-edge is hardly visible. The OCV1 Co pre-edge spectrum displays two separate peaks, corresponding to a Co^{2+} state (mixed with a Co^{3+} state due to the partial oxidation) and a nonlocal peak due to the Mn^{4+} near-neighbor.

Figure 3a presents the Mn K-edge HERFD XAS spectra of $\text{La}_2\text{CoMnO}_6$ thin films. One can observe small differences in intensity at the nonlocal state and the white line between the OCV1 and ex situ conditions. This could be (partly) due to coordination of the (oxy)hydroxide in OCV1. The ex situ Mn K-edge HERFD XAS approximately matches the white line energy position of MnO_2 .⁶² Figure 3b presents soft X-ray Mn 2p XAS of $\text{La}_2\text{CoMnO}_6$ thin films and Mn^{4+} 2p XAS charge-transfer multiplet simulations with parameters taken from ref 56. The well-matched ex situ Mn 2p XAS confirms the existence of Mn^{4+} in the $\text{La}_2\text{CoMnO}_6$ thin films. The Mn K pre-edge presents two peaks, where the lower energy position relates to 1s to 3d quadrupole transition while the higher energy position corresponds to nonlocal peaks.⁶³ These results indicate that under ex situ conditions, the 10 u.c. $\text{La}_2\text{CoMnO}_6$ thin films exhibit Co^{2+} – Mn^{4+} valence states in agreement with other studies.^{42–44} In the OCV1 condition, the Co (partly) oxidizes from +2 to +3, while the Mn-oxidation state of +4 remains constant.

Electrocatalytic Performances

Figure 4 shows the electrocatalytic performance of 10 u.c. $\text{La}_2\text{CoMnO}_6$ thin films. The presented electrochemical data in the OER regime with five well-reproducible cycles indicate stable electrocatalytic performance. The OER activity of 1 mA/cm² at an overpotential of ~ 480 mV is considerable regarding the smooth surface of the PLD-grown thin film.³⁶ The CV scan in the lower potential range (inset 1.27 to 1.57 V) with different

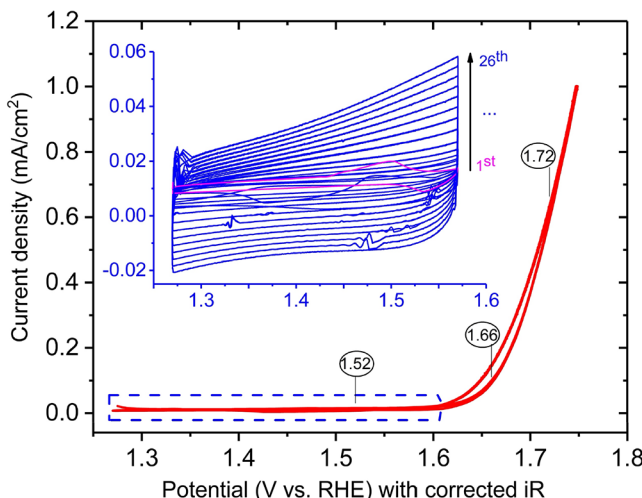


Figure 4. Electrocatalytic performance of the 10 u.c. $\text{La}_2\text{CoMnO}_6$ thin films, showing 5 cycles with a scan rate of 10 mV/s, with the inset showing 26 cycles within the Faraday region of 1.27 to 1.57 V with various scan rates from 10 to 500 mV; the labels of 1.52, 1.66, and 1.72 V denote the applied potentials during operando HERFD-XAS.

scan rates show no pronounced redox waves such as one might expect from an electrocatalytic $\text{Co}^{2+}/\text{3+}$ to $\text{Co}^{3+}/\text{4+}$ transition at a fixed redox potential.²⁸

Operando Potential-Dependent Co K-Edge Spectra

Figure 5a presents the operando potential-dependent Co K-edge HERFD XAS spectra. **Figure 5b** shows the enlarged Co pre-edge spectra. **Figure 5c** shows the corresponding operando difference spectra using the spectral data from the OCV1 spectrum as a reference. There are four trends observed: (1) the pre-edge peak maximum energy positively shifts and its intensity increases, (2) the pre-edge second peak at 7712.5 eV disappears,

(3) the white line intensity declines and the 1s to 4p edge shifts, and (4) the post-white line intensity increases at ~ 7735 eV. The extracted data on energy shifts, edge-rising (maximum), and intensity variations are shown in **Figure 6**.

Figure 6a presents that the operando potential-dependent Co K-edge in the white line declines and main edge energy shifts as a function of potential. **Figure 6b** shows the pre-edge intensity increase and energy shift with an increasing potential. These observations will be discussed in the Discussion section in detail.

Operando Potential-Dependent Mn K-Edge Spectra

Figure 7a presents the operando potential-dependent Mn K-edge HERFD XAS spectra. **Figure 7b** presents enlarged Mn pre-edges, indicating that the second peak at 6541.7 eV is increased under the applied potential. **Figure 7c** presents the operando difference spectra using reference OCV1 spectra. **Figure 7d** presents the quantitative pre-edge intensity changes at 6541.7 eV and main edge energy shifts at the maximum position.

Reversible K-Edge Spectra in OCV

Figure 8a presents Co K-edge HERFD XAS under open-circuit voltage conditions with sequences OCV1, OCV2, and OCV3 (details in the methods). Regardless of the applied moderate potential or higher potential (up to 0.93 V vs Ag/AgCl in **Figure S6**), the Co K-edge HERFD XAS spectra for OCV2 and OCV3 return to the same state as OCV1 after the potential is switched off. **Figure 8b** exhibits the corresponding derivative spectra. These observations show no significant changes in spectral shapes. **Figure 8c** presents Mn K-edge HERFD XAS under an open-circuit voltage, with measurements corresponding to OCV1, OCV2, and OCV3, analogous to the Co K-edge HERFD XAS OCV measurements. The Mn K-edge HERFD XAS spectra for both OCV2 and OCV3 revert to the OCV1 condition. **Figure 8d** shows the corresponding first derivative spectra with similar features across all of the conditions. All in all,

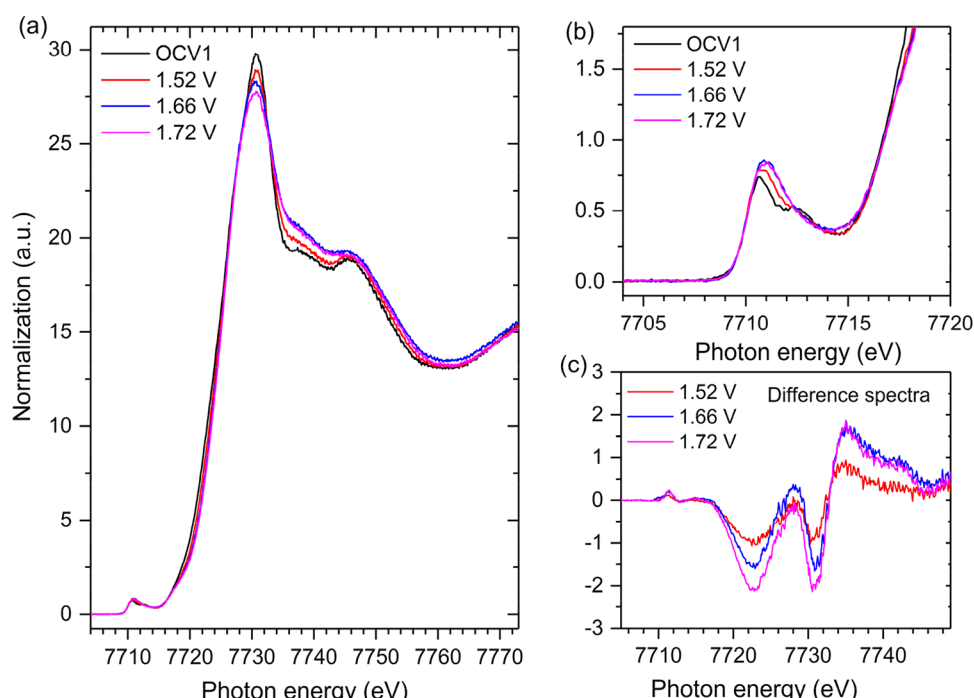


Figure 5. (a) Operando potential-dependent Co K-edge HERFD XAS spectra. (b) Enlarged Co pre-edges 1s to 3d. (c) Corresponding operando difference spectra relative to OCV1 reference.

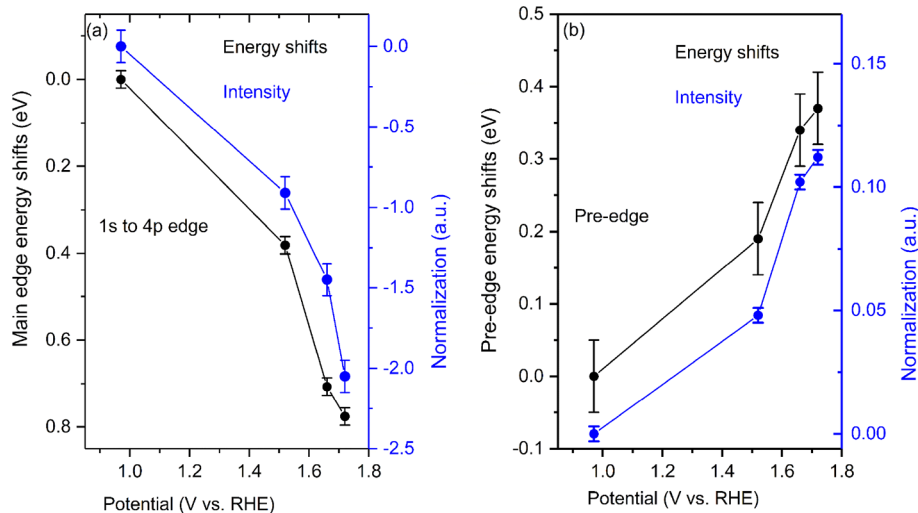


Figure 6. Extracted information from Figure 5; (a) operando voltage-dependent Co K-edge white line declines and main edge energy shifts, (b) pre-edge intensity increase and energy shifts.

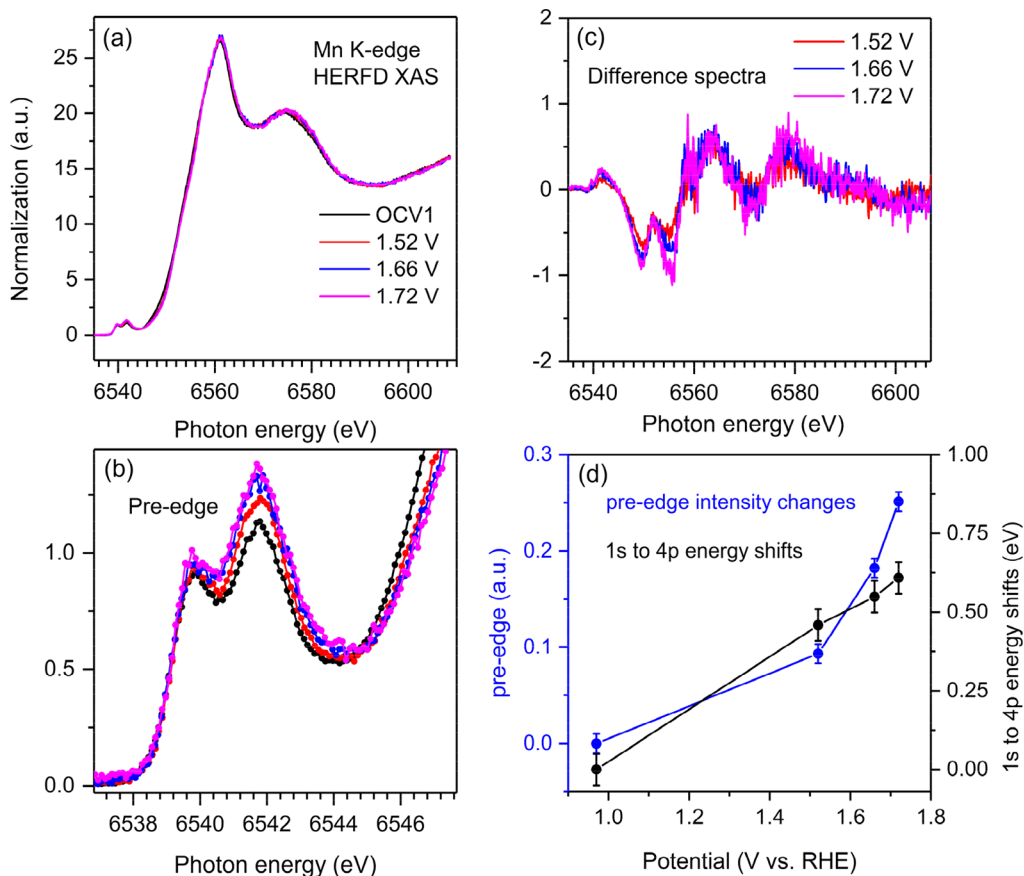


Figure 7. (a) The operando voltage-dependent Mn K-edge HERFD XAS spectra. (b) Enlarged Mn pre-edges with 1s to 3d quadrupole and nonlocal states. (c) The corresponding operando difference spectra relative to OCV1 reference. (d) The pre-edge intensity increases at 6541.7 eV and main edge energy shifts.

the spectra at OCV reveal full reversibility of the electrochemically induced changes in the (electronic) structure.

DISCUSSION

We observe that in the OCV1 condition, the whole 10 u.c. $\text{La}_2\text{CoMnO}_6$ thin films undergo a change, with the cobalt ions exhibiting a similar spectral fingerprint as Co^{3+} in CoOOH , as

shown in Figure 2. The Mn maintains a constant +4 valence state due to the effects of the near-zero or negative charge-transfer value Δ_{ct} .^{42,56} The discussion will focus on the spectral intensity and energy shifts relative to chemical shifts (or formal oxidation state) and covalence, particularly in relation to the intrinsic oxygen evolution reaction.

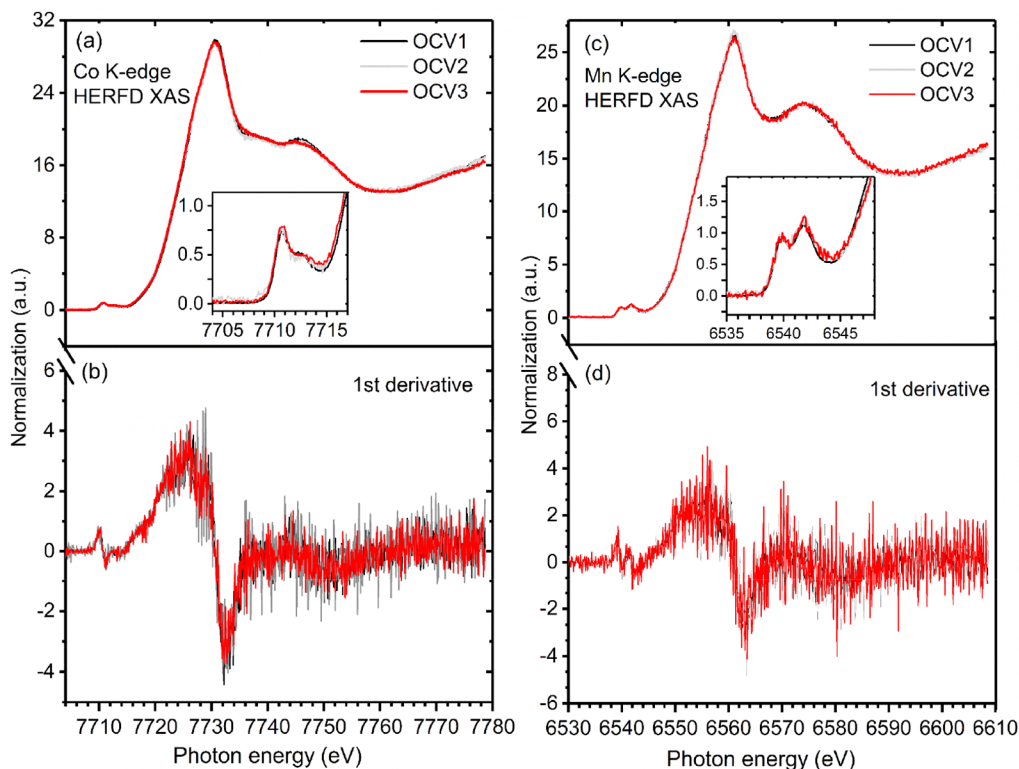


Figure 8. (a) Co K-edge HERFD XAS under open-circuit voltage (OCV) conditions and (b) corresponding first derivative spectra. (c) Mn K-edge HERFD XAS in open-circuit voltage (OCV) conditions and (d) corresponding to first derivative spectra.

The Relation between the 4p Band and the Metal Valences

The main edge of 1s XAS is the 1s to lowest p state transition, which probes the unoccupied 4p band. As discussed in the introduction, changes in the TM white line intensity reflect changes in the TM 4p character, indicating alterations in TM character in the 4p band, where the intensity is given by the amount of 4p character. We observe a clear decline in the Co K-edge white line with increasing potential (Figure 6a), which corresponds to a reduction in Co 4p character. This decline indicates an increase in cobalt 4p–oxygen 2p bonding, which in turn indicates an oxidation of the $\text{Co}^{2+/\text{3}+}$ ions. In contrast, the Mn K-edge white line intensity does not exhibit visible changes, which implies that the amount of Mn 4p character is constant, which in turn implies a constant Mn^{4+} oxidation state.

Additionally, both the Co K-edge and Mn K-edge 4p bands show a shift to higher energy (Figures 6a and 7d), indicating that the average oxidation state of the TM ions increases. The edge shift is approximately 0.60 and 0.80 eV for Mn and Co, respectively, which indicates an average valence increase of $\sim 0.70/3.2 \approx 0.20$. The valence of Mn does not change indicating that the valence of Co increased by 0.4 between the OCV (0.97 V vs RHE) and a potential of 1.72 V vs RHE. In line with the electrochemical behavior at the lower potential, only moderate Co valence state occurs below 1.6 V vs RHE, while a more rapid Co valence state with increasing potential occurs after the onset of OER. The increase in valence stabilizes under higher potentials (Figure S6).

The Relation between the 3d Band and the Metal Valences

We observed the following for the Co pre-edge XAS: (1) A positive shift in the pre-edge energy relative to that of OCV1, (2) an increase in intensity (Figure 6b), and (3) disappearance of the peak localized at 7712.5 eV (related to nonlocal states)

under operando conditions (Figure 5b). We interpret these changes due to the oxidation of the Co ions toward higher oxidation states combined with an increased distortion of the octahedral symmetry. The symmetry distortions allow dipole–quadrupole mixing, which allows the transfer of intensity of the nonlocal (dipole) peak to the local (quadrupole) peak. In addition, the partial oxidation shifts the local peak to higher energy. For the Mn pre-edge XAS, the energy position of the local peak remains constant, in line with the constant oxidation state inferred from the constant white line intensity. In contrast, the intensity of the nonlocal peak increases (Figure 7), consistent with a constant Mn^{4+} valence and shorter average Co–O–Mn distances.

Reversibility

The operando Co K-edge and Mn K-edge HERFD XAS spectra in the solid–liquid (OCV) conditions revert to the OCV1 environment (Figure 8). When a slightly higher voltage is reapplied, the effects on intensity and energy shifts for both the 3d and 4p bands are reproducible (Figures S6 and S7).

The potential-induced changes in Co valence states dominate, suggesting that Co sites are the primary active centers during OER. This observation is consistent with prior studies on perovskite cobaltites⁶⁴ and provides mechanistic insight into why Co, rather than Mn, governs the catalytic response. Simultaneous energy-position shifts of both Co and Mn across the entire layer suggest that the lattice, not just the surface, participates in the OER mechanism. This lattice response may rationalize Density Functional Theory calculations for the bulk¹⁷ correlate well with the experimental activity.

CONCLUSION

We conducted a study on operando Co and Mn K-edge HERFD XAS of 10 u.c. $\text{La}_2\text{CoMnO}_6$ thin films were observed during the electrocatalytic oxygen evolution reaction in a 0.1 M KOH solution. The intensity of the Co K-edge white line revealed a formation from Co^{2+} to (oxy)hydroxides partly oxidized to Co^{3+} in the alkaline environment (without potential), while the Mn K-edge white line intensity showed that Mn retained its oxidation state of +4. The position of the main K-edge energy increased both Co and Mn, indicating that the average valence increased by ~0.20 for an applied potential increase of 1.72 V, which implies that the Co valence increased by ~0.4, while the Mn valence remained constant.

The pre-edge confirms the partial oxidation to a higher oxidation state and further indicates an increased symmetry distortion of the TM–O octahedra. Due to the presence of high-valent Mn ions, the nonlocal peak is relatively strong.

The HERFD XAS spectra were reversible when the applied potentials were switched off, returning to the state observed under open-circuit conditions. These findings underscore the crucial role of relative changes of the Co and Mn valences in intrinsic oxygen evolution, highlighting valence as a key descriptor for the OER mechanism and emphasizing the value of HERFD XAS in operando near-surface studies.

ASSOCIATED CONTENT

Supporting Information

The Supporting Information is available free of charge at <https://pubs.acs.org/doi/10.1021/jacs.Sc14062>.

Additional tables and figures containing EIS, Mn K-edge HERFD XAS of MnO before and after operando experiments, homogeneity and beam damage studies of K-edge HERFD XAS, Co K-edge HERFD XAS first derivative spectra, operando higher voltage-dependent Co and Mn K-edge HERFD XAS spectra, XRD data, and AFM image ([PDF](#))

AUTHOR INFORMATION

Corresponding Authors

Qijun Che – Debye Institute for Nanomaterials Science, Utrecht University, 3584 CG Utrecht, The Netherlands; SLAC National Accelerator Laboratory, Menlo Park, California 94025, United States; orcid.org/0009-0008-5805-7727; Email: q.che@uu.nl

Christoph Baeumer – MESA+ Institute for Nanotechnology, University of Twente, Enschede 7500 AE, The Netherlands; orcid.org/0000-0003-0008-514X; Email: c.baeumer@utwente.nl

Frank M. F. de Groot – Debye Institute for Nanomaterials Science, Utrecht University, 3584 CG Utrecht, The Netherlands; orcid.org/0000-0002-1340-2186; Email: F.M.F.deGroot@uu.nl

Authors

Iris C. G. van den Bosch – MESA+ Institute for Nanotechnology, University of Twente, Enschede 7500 AE, The Netherlands; orcid.org/0009-0004-6249-8729

Jelle R. H. Ruiters – MESA+ Institute for Nanotechnology, University of Twente, Enschede 7500 AE, The Netherlands

Yuang Piao – Debye Institute for Nanomaterials Science, Utrecht University, 3584 CG Utrecht, The Netherlands

Pieter Glatzel – ESRF, The European Synchrotron, Grenoble 38043, France; orcid.org/0000-0001-6532-8144

Danilo Kühn – Institut für Methoden und Instrumentierung der Forschung mit Synchrotronstrahlung, Helmholtz-Zentrum Berlin für Materialien und Energie GmbH, Berlin 12489, Germany; orcid.org/0009-0008-4776-4928

Complete contact information is available at: <https://pubs.acs.org/10.1021/jacs.Sc14062>

Notes

The authors declare no competing financial interest.

ACKNOWLEDGMENTS

We thank the ESRF ID26 beamline staff for assistance with the operando experimental setup. Vadim Ratovskii is acknowledged for help with the PLD thin film samples, and Ellen M. Kiens for performing the XRD and AFM measurements of the films. We are grateful to the Helmholtz-Zentrum Berlin für Materialien und Energie for the allocation of synchrotron beamtime (October 2024). We acknowledge ESRF and BESSY II for travel funding support. The authors declare that no additional funding was received for this work.

REFERENCES

- (1) Vogt, E. T. C.; Weckhuysen, B. M. The refinery of the future. *Nature* **2024**, *629* (8011), 295–306.
- (2) Hansen, O.; Seger, B.; Vesborg, P. C. K.; Chorkendorff, I. A quick look at how photoelectrodes work. *Science* **2015**, *350* (6264), 1030–1031.
- (3) Grimaud, A.; Diaz-Morales, O.; Han, B.; Hong, W. T.; Lee, Y.-L.; Giordano, L.; Stoerzinger, K. A.; Koper, M. T. M.; Shao-Horn, Y. Activating lattice oxygen redox reactions in metal oxides to catalyse oxygen evolution. *Nat. Chem.* **2017**, *9* (5), 457–465.
- (4) Favaro, M.; Yang, J.; Nappini, S.; Magnano, E.; Toma, F. M.; Crumlin, E. J.; Yano, J.; Sharp, I. D. Understanding the oxygen evolution reaction mechanism on CoO_x using operando ambient-pressure X-ray photoelectron spectroscopy. *J. Am. Chem. Soc.* **2017**, *139* (26), 8960–8970.
- (5) Dau, H.; Limberg, C.; Reier, T.; Risch, M.; Roggan, S.; Strasser, P. The mechanism of water oxidation: from electrolysis via homogeneous to biological catalysis. *ChemCatChem* **2010**, *2* (7), 724–761.
- (6) Suntivich, J.; May, K. J.; Gasteiger, H. A.; Goodenough, J. B.; Shao-Horn, Y. A perovskite oxide optimized for oxygen evolution catalysis from molecular orbital principles. *Science* **2011**, *334* (6061), 1383–1385.
- (7) Burke, M. S.; Enman, L. J.; Batcheller, A. S.; Zou, S.; Boettcher, S. W. Oxygen evolution reaction electrocatalysis on transition metal oxides and (oxy)hydroxides: Activity trends and design principles. *Chem. Mater.* **2015**, *27* (22), 7549–7558.
- (8) Gerken, J. B.; McAlpin, J. G.; Chen, J. Y. C.; Rigsby, M. L.; Casey, W. H.; Britt, R. D.; Stahl, S. S. Electrochemical water oxidation with cobalt-based electrocatalysts from pH 0–14: the thermodynamic basis for catalyst structure, stability, and activity. *J. Am. Chem. Soc.* **2011**, *133* (36), 14431–14442.
- (9) Man, I. C.; Su, H.; Calle-Vallejo, F.; Hansen, H. A.; Martínez, J. I.; Inoglu, N. G.; Kitchin, J.; Jaramillo, T. F.; Nørskov, J. K.; Rossmeisl, J. Universality in oxygen evolution electrocatalysis on oxide surfaces. *ChemCatChem* **2011**, *3* (7), 1159–1165.
- (10) Rossmeisl, J.; Qu, Z.-W.; Zhu, H.; Kroes, G.-J.; Nørskov, J. K. Electrolysis of water on oxide surfaces. *J. Electroanal. Chem.* **2007**, *607* (1–2), 83–89.
- (11) Nørskov, J. K.; Rossmeisl, J.; Logadottir, A.; Lindqvist, L.; Kitchin, J. R.; Bligaard, T.; Jónsson, H. Origin of the overpotential for oxygen reduction at a fuel-cell cathode. *J. Phys. Chem. B* **2004**, *108* (46), 17886–17892.

- (12) Giordano, L.; Han, B.; Risch, M.; Hong, W. T.; Rao, R. R.; Stoerzinger, K. A.; Shao-Horn, Y. PH dependence of OER activity of oxides: current and future perspectives. *Catal. Today* **2016**, *262*, 2–10.
- (13) Matsumoto, Y.; Manabe, H.; Sato, E. Oxygen evolution on $\text{La}_{1-x}\text{Sr}_x\text{CoO}_3$ electrodes in alkaline solutions. *J. Electrochem. Soc.* **1980**, *127* (4), 811–814.
- (14) Trześniewski, B. J.; Diaz-Morales, O.; Vermaas, D. A.; Longo, A.; Bras, W.; Koper, M. T. M.; Smith, W. A. In Situ observation of active oxygen species in Fe-containing Ni-based oxygen evolution catalysts: the effect of PH on electrochemical activity. *J. Am. Chem. Soc.* **2015**, *137* (48), 15112–15121.
- (15) Grimaud, A.; May, K. J.; Carlton, C. E.; Lee, Y.-L.; Risch, M.; Hong, W. T.; Zhou, J.; Shao-Horn, Y. Double perovskites as a family of highly active catalysts for oxygen evolution in alkaline solution. *Nat. Commun.* **2013**, *4* (1), 2439.
- (16) Suntivich, J.; Hong, W. T.; Lee, Y. L.; Rondinelli, J. M.; Yang, W.; Goodenough, J. B.; Dabrowski, B.; Freeland, J. W.; Shao-Horn, Y. Estimating hybridization of transition metal and oxygen states in perovskites from O K-edge X-ray absorption spectroscopy. *J. Phys. Chem. C* **2014**, *118* (4), 1856–1863.
- (17) Calle-Vallejo, F.; Diaz-Morales, O. A.; Kolb, M. J.; Koper, M. T. M. Why is bulk thermochemistry a good descriptor for the electrocatalytic activity of transition metal oxides? *ACS Catal.* **2015**, *5* (2), 869–873.
- (18) Rong, X.; Parolin, J.; Kolpak, A. M. A Fundamental relationship between reaction mechanism and stability in metal oxide catalysts for oxygen evolution. *ACS Catal.* **2016**, *6* (2), 1153–1158.
- (19) Hibbert, D. B.; Churchill, C. R. Kinetics of the electrochemical evolution of isotopically enriched gases. Part 2. $-^{18}\text{O}^{16}\text{O}$ evolution on NiCo_2O_4 and $\text{Li}_x\text{Co}_{3-x}\text{O}_4$ in alkaline solution. *J. Chem. Soc., Faraday Trans. 1* **1984**, *80* (7), 1965–1975.
- (20) Mavros, M. G.; Tsuchimochi, T.; Kowalczyk, T.; McIsaac, A.; Wang, L.-P.; Voorhis, T. V. What can density functional theory tell us about artificial catalytic water splitting? *Inorg. Chem.* **2014**, *53* (13), 6386–6397.
- (21) Wang, L.-P.; Van Voorhis, T. Direct-coupling O_2 bond forming a pathway in cobalt oxide water oxidation catalysts. *J. Phys. Chem. Lett.* **2011**, *2* (17), 2200–2204.
- (22) Betley, T. A.; Wu, Q.; Van Voorhis, T.; Nocera, D. G. Electronic design criteria for O–O bond formation via metal–oxo complexes. *Inorg. Chem.* **2008**, *47* (6), 1849–1861.
- (23) Simböck, J.; Ghiasi, M.; Schönebaum, S.; Simon, U.; de Groot, F. M. F.; Palkovits, R. Electronic parameters in cobalt-based perovskite-type oxides as descriptors for chemocatalytic reactions. *Nat. Commun.* **2020**, *11* (1), 652.
- (24) Timoshenko, J.; Roldan Cuenya, B. In Situ/operando electrocatalyst characterization by X-ray absorption spectroscopy. *Chem. Rev.* **2021**, *121* (2), 882–961.
- (25) Song, S.; Zhou, J.; Su, X.; Wang, Y.; Li, J.; Zhang, L.; Xiao, G.; Guan, C.; Liu, R.; Chen, S.; Lin, H.-J.; Zhang, S.; Wang, J.-Q. Operando X-ray spectroscopic tracking of self-reconstruction for anchored nanoparticles as high-performance electrocatalysts towards oxygen evolution. *Energy Environ. Sci.* **2018**, *11* (10), 2945–2953.
- (26) Huang, J.; Chen, J.; Yao, T.; He, J.; Jiang, S.; Sun, Z.; Liu, Q.; Cheng, W.; Hu, F.; Jiang, Y.; Pan, Z.; Wei, S. CoOOH nanosheets with high mass activity for water oxidation. *Angew. Chem., Int. Ed.* **2015**, *54* (29), 8722–8727.
- (27) Su, X.; Wang, Y.; Zhou, J.; Gu, S.; Li, J.; Zhang, S. Operando spectroscopic identification of active sites in NiFe Prussian blue analogues as electrocatalysts: activation of oxygen atoms for oxygen evolution reaction. *J. Am. Chem. Soc.* **2018**, *140* (36), 11286–11292.
- (28) Mefford, J. T.; Akbashev, A. R.; Kang, M.; Bentley, C. L.; Gent, W. E.; Deng, H. D.; Alsem, D. H.; Yu, Y. S.; Salmon, N. J.; Shapiro, D. A.; Unwin, P. R.; Chueh, W. C. Correlative operando microscopy of oxygen evolution electrocatalysts. *Nature* **2021**, *593* (7857), 67–73.
- (29) Al Samarai, M.; Hahn, A. W.; Beheshti Askari, A.; Cui, Y. T.; Yamazoe, K.; Miyawaki, J.; Harada, Y.; Rüdiger, O.; Debeer, S. Elucidation of structure-activity correlations in a nickel manganese oxide oxygen evolution reaction catalyst by operando Ni L-edge X-ray absorption spectroscopy and 2p3d resonant inelastic X-ray scattering. *ACS Appl. Mater. Interfaces* **2019**, *11* (42), 38595–38605.
- (30) Huang, Y. C.; Chen, W.; Xiao, Z.; Hu, Z.; Lu, Y. R.; Chen, J. L.; Chen, C. L.; Lin, H. J.; Chen, C. T.; Arul, K. T.; Wang, S.; Dong, C. L.; Chou, W. C. In Situ/operando soft X-ray spectroscopic identification of a Co^{4+} intermediate in the oxygen evolution reaction of defective Co_3O_4 nanosheets. *J. Phys. Chem. Lett.* **2022**, *13* (35), 8386–8396.
- (31) Chen, J. Y. C.; Dang, L.; Liang, H.; Bi, W.; Gerken, J. B.; Jin, S.; Alp, E. E.; Stahl, S. S. Operando analysis of NiFe and Fe oxyhydroxide electrocatalysts for water oxidation: detection of Fe^{4+} by Mössbauer spectroscopy. *J. Am. Chem. Soc.* **2015**, *137* (48), 15090–15093.
- (32) Bisogni, V.; Catalano, S.; Green, R. J.; Gibert, M.; Scherwitzl, R.; Huang, Y.; Strocov, V. N.; Zubko, P.; Balandeh, S.; Triscone, J. M.; Sawatzky, G.; Schmitt, T. Ground-state oxygen holes and the metal-insulator transition in the negative charge-transfer rare-earth nickelates. *Nat. Commun.* **2016**, *7*, 13017–13018.
- (33) Ushakov, A. V.; Streletsov, S. V.; Khomskii, D. I. Crystal field splitting in correlated systems with negative charge-transfer gap. *J. Phys.: Condens. Matter* **2011**, *23* (44), 445601.
- (34) Abbate, M.; Zampieri, G.; Okamoto, J.; Fujimori, A.; Kawasaki, S.; Takano, M. X-ray absorption of the negative charge-transfer material $\text{SrFe}_{1-x}\text{Co}_x\text{O}_3$. *Phys. Rev. B* **2002**, *65* (16), 165120.
- (35) De Groot, F.; Kotani, A. *Core Level Spectroscopy of Solids*; CRC Press, 2008.
- (36) Füngerlings, A.; Wohlgemuth, M.; Antipin, D.; van der Minne, E.; Kiens, E. M.; Villalobos, J.; Risch, M.; Gunkel, F.; Pentcheva, R.; Baeumer, C. Crystal-Facet-Dependent Surface Transformation Dictates the Oxygen Evolution Reaction Activity in Lanthanum Nickelate. *Nat. Commun.* **2023**, *14* (1), 8284.
- (37) Weber, M. L.; Gunkel, F. Epitaxial catalysts for oxygen evolution reaction: model systems and beyond. *J. Phys.: Energy* **2019**, *1*, 031001.
- (38) Antipin, D.; Risch, M. Trends of epitaxial perovskite oxide films catalyzing the oxygen evolution reaction in alkaline media. *J. Phys.: Energy* **2020**, *2*, 032003.
- (39) Stoerzinger, K. A.; Risch, M.; Suntivich, J.; Lü, W. M.; Zhou, J.; Biegalski, M. D.; Christen, H. M.; Ariando; Venkatesan, T.; Shao-Horn, Y. Oxygen electrocatalysis on (001)-oriented manganese perovskite films: Mn valency and charge transfer at the nanoscale. *Energy Environ. Sci.* **2013**, *6* (5), 1582–1588.
- (40) Baeumer, C.; Li, J.; Lu, Q.; Liang, A. Y. L.; Jin, L.; Martins, H. P.; Duchoň, T.; Glöß, M.; Gericke, S. M.; Wohlgemuth, M. A.; Giesen, M.; Penn, E. E.; Dittmann, R.; Gunkel, F.; Waser, R.; Bajdich, M.; Nemšák, S.; Mefford, J. T.; Chueh, W. C. Tuning electrochemically driven surface transformation in atomically flat LaNiO_3 thin films for enhanced water electrolysis. *Nat. Mater.* **2021**, *20* (5), 674–682.
- (41) Che, Q.; van den Bosch, I. C. G.; Le, P. T. P.; Lazemi, M.; van der Minne, E.; Birkhölzer, Y. A.; Nunnenkamp, M.; Peerlings, M. L. J.; Safanova, O. V.; Nachtegaal, M.; Koster, G.; Baeumer, C.; de Jongh, P.; de Groot, F. M. F. In Situ X-ray absorption spectroscopy of LaFeO_3 and $\text{LaFeO}_3/\text{LaNiO}_3$ thin films in the electrocatalytic oxygen evolution reaction. *J. Phys. Chem. C* **2024**, *128* (13), 5515–5523.
- (42) Burnus, T.; Hu, Z.; Hsieh, H. H.; Joly, V. L. J.; Joy, P. A.; Havercort, M. W.; Wu, H.; Tanaka, A.; Lin, H. J.; Chen, C. T.; Tjeng, L. H. Local electronic structure and magnetic properties of $\text{LaMn}_{0.5}\text{Co}_{0.5}\text{O}_3$ studied by X-ray absorption and magnetic circular dichroism spectroscopy. *Phys. Rev. B* **2008**, *77* (12), 125124.
- (43) Wang, H.; Gazquez, J.; Frontera, C.; Chisholm, M. F.; Pomar, A.; Martinez, B.; Mestres, N. Spontaneous cationic ordering in chemical-solution-grown $\text{La}_2\text{CoMnO}_6$ double perovskite thin films. *NPG Asia Mater.* **2019**, *11* (1), 44.
- (44) Guo, H. Z.; Gupta, A.; Calvarese, T. G.; Subramanian, M. A. Structural and magnetic properties of epitaxial thin films of the ordered double perovskite $\text{La}_2\text{CoMnO}_6$. *Appl. Phys. Lett.* **2006**, *89* (26), 262503.
- (45) de Groot, F. M. F.; Havercort, M. W.; Elnaggar, H.; Juhin, A.; Zhou, K.-J.; Glatzel, P. Resonant inelastic X-ray scattering. *Nat. Rev. Methods Primers* **2024**, *4* (1), 45.

- (46) Hämäläinen, K.; Siddons, D. P.; Hastings, J. B.; Berman, L. E. Elimination of the inner-shell lifetime broadening in X-ray-absorption spectroscopy. *Phys. Rev. Lett.* **1991**, *67* (20), 2850.
- (47) Wong, J.; Lytle, F. W.; Messmer, R. P.; Maylotte, D. H. K-edge absorption spectra of selected vanadium compounds. *Phys. Rev. B* **1984**, *30* (10), 5596–5610.
- (48) Grioni, M.; Goedkoop, J. B.; Schoorl, R.; de Groot, F. M. F.; Fuggle, J. C.; Schäfers, F.; Koch, E. E.; Rossi, G.; Esteva, J.-M.; Karnataka, R. C. Studies of copper valence states with Cu L₃ x-ray-absorption spectroscopy. *Phys. Rev. B* **1989**, *39* (3), 1541–1545.
- (49) Yuan, H.; Nguyen, M.; Hammer, T.; Koster, G.; Rijnders, G.; ten Elshof, J. E. Synthesis of KCa₂Nb₃O₁₀ crystals with varying grain sizes and their nanosheet monolayer films as seed layers for PiezoMEMS applications. *ACS Appl. Mater. Interfaces* **2015**, *7* (49), 27473–27478.
- (50) Nečas, D.; Klapetek, P. Gwyddion An open-source software for SPM data analysis. *Open Phys.* **2012**, *10* (1), 181–188.
- (51) Niu, S.; Li, S.; Du, Y.; Han, X.; Xu, P. How to Reliably report the overpotential of an electrocatalyst. *ACS Energy Lett.* **2020**, *5*, 1083–1087.
- (52) Gauthier, C.; Solé, V. A.; Signorato, R.; Goulon, J.; Moguiline, E. The ESRF beamline ID26: X-ray absorption on ultra dilute sample. *J. Synchrotron Radiat.* **1999**, *6* (3), 164–166.
- (53) Glatzel, P.; Harris, A.; Marion, P.; Sikora, M.; Weng, T.-C.; Guilloud, C.; Lafuerza, S.; Rovezzi, M.; Detlefs, B.; Ducotté, L. The Five-Analyzer Point-to-Point Scanning Crystal Spectrometer at ESRF ID26. *J. Synchrotron Radiat.* **2021**, *28*, 362–371.
- (54) De Groot, F. M. F. Dips and peaks in fluorescence yield X-ray absorption are due to state-dependent decay. *Nat. Chem.* **2012**, *4* (10), 766–767.
- (55) De Groot, F. M. F.; Glatzel, P.; Bergmann, U.; van Aken, P. A.; Barrea, R. A.; Klemme, S.; Hävecker, M.; Knop-Gericke, A.; Heijboer, W. M.; Weckhuysen, B. M. 1s2p Resonant inelastic X-ray scattering of iron oxides. *J. Phys. Chem. B* **2005**, *109* (44), 20751–20762.
- (56) Che, Q.; Ghiasi, M.; Braglia, L.; Peerlings, M. L. J.; Mauri, S.; Torelli, P.; de Jongh, P.; de Groot, F. M. F. Operando Soft X-ray Absorption of LaMn_{1-x}Co_xO₃ Perovskites for CO Oxidation. *ACS Catal.* **2024**, *14*, 11243–11251.
- (57) Friebel, D.; Bajdich, M.; Yeo, B. S.; Louie, M. W.; Miller, D. J.; Sanchez Casalongue, H.; Mbuga, F.; Weng, T. C.; Nordlund, D.; Sokaras, D.; Alonso-Mori, R.; Bell, A. T.; Nilsson, A. On the chemical state of Co oxide electrocatalysts during alkaline water splitting. *Phys. Chem. Chem. Phys.* **2013**, *15* (40), 17460–17467.
- (58) De Groot, F.; Vankó, G.; Glatzel, P. The 1s X-ray absorption pre-edge structures in transition metal oxides. *J. Phys.: Condens. Matter* **2009**, *21* (10), 104207.
- (59) Shulman, G. R.; Yafet, Y.; Eisenberger, P.; Blumberg, W. E. Observations and interpretation of X-ray absorption edges in iron compounds and proteins. *Proc. Natl. Acad. Sci. U.S.A.* **1976**, *73* (5), 1384–1388.
- (60) Wang, R.-P.; Huang, M.-J.; Hariki, A.; Okamoto, J.; Huang, H.-Y.; Singh, A.; Huang, D.-J.; Nagel, P.; Schuppler, S.; Haarman, T.; Liu, B.; de Groot, F. M. F. Analyzing the local electronic structure of Co₃O₄ using 2p3d resonant inelastic X-ray scattering. *J. Phys. Chem. C* **2022**, *126* (20), 8752–8759.
- (61) Juhin, A.; De Groot, F.; Vankó, G.; Calandra, M.; Brouder, C. Angular dependence of core hole screening in LiCoO₂: A DFT+U calculation of the oxygen and cobalt K-edge X-ray absorption spectra. *Phys. Rev. B* **2010**, *81* (11), 115115.
- (62) García, J.; Subías, G.; Blasco, J. XAS studies on mixed valence oxides. In *X-ray absorption and X-ray emission spectroscopy*; Van Bokhoven, J. A., Lamberti, C., Eds.; Wiley, 2016.
- (63) Lafuerza, S.; García, J.; Subías, G.; Blasco, J.; Glatzel, P. High-resolution Mn K-edge X-ray emission and absorption spectroscopy study of the electronic and local structure of the three different phases in Nd_{0.5}Sr_{0.5}MnO₃. *Phys. Rev. B* **2016**, *93* (20), 205108.
- (64) Kante, M. V.; Weber, M. L.; Ni, S.; van den Bosch, I. C. G.; van der Minne, E.; Heymann, L.; Falling, L. J.; Gauquelin, N.; Tsvetanova, M.; Cunha, D. M.; Koster, G.; Gunkel, F.; Nemšák, S.; Hahn, H.; Velasco Estrada, L. V.; Baeumer, C. A High-entropy oxide as high-
- activity electrocatalyst for water oxidation. *ACS Nano* **2023**, *17* (6), 5329–5339.

CAS BIOFINDER DISCOVERY PLATFORM™

ELIMINATE DATA SILOS. FIND WHAT YOU NEED, WHEN YOU NEED IT.

A single platform for relevant, high-quality biological and toxicology research

Streamline your R&D

CAS 
A division of the
American Chemical Society